Electronic Supplementary Information (ESI) for

Constructing oxygen vacancies by doping Mo into spinel Co_3O_4 to trigger fast oxide path mechanism for acidic oxygen evolution reaction

Lang Sun, Min Feng, Yang Peng, Xu Zhao, Yiqun Shao, Xin Yue* and Shaoming Huang*

Guangzhou Key Laboratory of Low-Dimensional Materials and Energy Storage Devices, Collaborative Innovation Center of Advanced Energy Materials, School of Materials and Energy, Guangdong University of Technology, Guangzhou, 510006, P. R. China.

E-mail: xinyue@gdut.edu.cn (X. Y.); smhuang@gdut.edu.cn (S. H.).

Experimental Section

Synthesis

Chemicals: Cobalt nitrate hexahydrate ($Co(NO_3)_2 \cdot 6H_2O$, AR), ammonium molybdate tetrahydrate (($NH_4)_6Mo_7O_{24} \cdot 4H_2O$, AR) and sodium hydroxide (NaOH, AR) were purchased from Shanghai Macklin Biochemical Co., Ltd. Hydrochloric acid (HCl, AR) was purchased from Chengdu Cologne Chemical Co., Ltd. Ethanol (C_2H_6O, AR) was purchased from Tianjin Chemo Chemical Reagent Co., Ltd. Deionized (DI) water was homemade. Carbon paper (CP) was purchased from Hubei Rocktech Instrument Co., Ltd.

Synthesis of Mo-doped oxygen vacancies enriched Co_3O_4 (V_O-$Mo_XCo_{3-X}O_4$): Firstly, NaOH was dissolved in 50 mL of deionized water until the pH value was adjusted to 12. Secondly, $Co(NO_3)_2 \cdot 6H_2O$ (0.100 mmol) and $(NH_4)_6Mo_7O_{24} \cdot 4H_2O$ (0.400 mmol) were dissolved into 50 mL of the resulting solution and stirred for 60 min. Then, the resulting mixture was transferred into a polytetrafluoroethylene-lined autoclave (100

mL), Subsequently, it was heat treated in an electric oven for 6 h at 180 ℃. After cooling to room temperature, the resulting product was washed six times with deionized water and ethanol, followed by drying in a vacuum oven at 60 °C for 24 h. Finally, the resulting product was annealed in an air atmosphere at 300 °C for 2 h.

Synthesis of pure Co_3O_4: The synthesis process was the same as V_O-$Mo_XCo_{3-X}O_4$, except that no precursor of Mo was used.

Electrochemical measurement

For electrochemical measurement, the electrocatalyst was dispersed in 0.9 mL ethanol + 0.1 mL Nafion (0.5 wt%, DuPont) mixture by ultrasonic treating 24 h to form a well-dispersed catalyst ink and then it was drop-coated onto a carbon paper (CP, 1 cm × 1 cm) electrode for testing. All electrochemical measurements were performed on an Autolab PGSTAT204 electrochemical constant potential meter. The electrochemical measurements were carried out in a typical three-electrode system, with a graphite rod as the counter electrode, a reversible hydrogen electrode as the reference electrode, and carbon paper drop-coated with V_O-$Mo_XCo_{3-X}O_4$ or Co_3O_4 with a catalyst loading of 5 mg cm^{-2} as a working electrode. Electrochemical tests were performed on commercial Ir/C catalysts and blank carbon paper as comparisons. Polarization curves were tested at 25 °C in 0.1 M $HClO_4$ solution with a scan rate of 5 mV s^{-1}. All polarization curves were *iR*-corrected.

Electrochemical *in situ* FT-IR measurements were carried out on a Nicolet IS50 FT-IR spectrometer, assisted by a PIKE VeeMAX III variable angle sampling accessory (Shanghai Linglu Instrument Co. Ltd) and a liquid nitrogen cooled MCT detector. In the Spectro electrochemical three-electrode cell, a glassy carbon electrode was used as the working electrode, and a platinum wire and silver/silver chloride electrode were used as the counter electrode and reference electrode, respectively. The glassy carbon electrode pressed a drop of carbon paper coated with catalyst material (catalyst loading of 5 mg cm^{-2}) onto the IR window to form a thin layer (1-10 μm) of electrolyte. Then, the IR beam passed through the optical window through the thin layer of electrolyte, and reflected IR light on the surface of the electrode. Finally, the IR

detector was reached to collect the signal. 0.1 M $HClO_4$ was used as the electrolyte for the OER test. The test procedure was performed on an iviumstat electrochemical workstation by raising the electrode potential from OCP to 1.9 V *vs*. RHE and then recording the IR spectra.

Electrochemical *in situ* Raman measurements were performed on a Renishaw Via Qontor laser micro confocal Raman spectrometer. An electrochemical *in situ* Raman H-type spectral cell (Beijing Scistar Technology Co. Ltd.) was used for *in situ* Raman spectroscopy during electrochemical OER catalysis. Electrochemical testing of OER was performed on a typical three-electrode system at a typical three-electrode on an iviumstat electrochemical workstation. Catalyst-loaded carbon paper (area 1 cm^2) was used as the working electrode. Silver/silver chloride and graphite rod electrodes were used as reference and counter electrodes, respectively. The catalyst was electrochemically activated before the *in situ* electrochemical Raman experiments. Activation was performed in a potential window of (1.3 to 1.9V *vs*. RHE) with a scan rate of 50 mV s^{-1} until the CV curve stabilized. Time-varying experimental Raman spectra were performed at different potentials and Raman spectra were collected.

Characterizations.

X-ray diffraction (XRD) measurements were taken on a Rigaku SmartLab 9 kW x-ray diffractometer. Scanning electron microscopy (SEM) characterizations were carried out on a ThermoFisher Apero C scanning electron microscope. Transmission electron microscopy (TEM) measurements were performed on an FEI Talos F200S 200kV scanning/transmission electron microscope. X-ray photoelectron spectroscopy (XPS) characterizations were carried out on a Thermo Fisher Escalab 250Xi x-ray photoelectron spectrometer. Raman spectroscopy was performed on a Renishaw plc Raman spectrometer. Electron paramagnetic resonance (EPR) measurements were performed on a Bruker A300 electron paramagnetic resonance popper. Fourier transform infrared spectroscopy (FT-IR) characterizations were carried out on a Nicolet IS50 FT-IR spectrometer.

X-ray absorption fine structures characterizations were performed on at Co K-edge of various composites at room temperature in the transmission mode with silicon drift

fluorescence detector at beamline TLS07A1 of National Synchrotron Radiation Research Center (NSRRC) operated with a Si (111) double crystal monochromator. The synchrotron was detected at 1.5 GeV and 250 mA. Data reduction, data analysis, and EXAFS fitting were performed and analyzed with the Athena and Artemis programs of the Demeter data analysis packages that utilize the FEFF6 program to fit the EXAFS data.[S1, S2] The energy calibration of the sample was conducted through standard and Co foil, which as a reference was simultaneously measured. A linear function was subtracted from the pre-edge region, then the edge jump was normalized using Athena software. The $\chi(k)$ data were isolated by subtracting a smooth, third-order polynomial approximating the absorption background of an isolated atom. The k^3-weighted $\chi(k)$ data were Fourier transformed after applying a Hanning window function (Δk = 1.0). For EXAFS modeling, the global amplitude EXAFS (CN, R, σ^2 and ΔE_0) was obtained by nonlinear fitting, with least-squares refinement, of the EXAFS equation to the Fourier-transformed data in R-space, using Artemis software, EXAFS of the Co foil are fitted and the obtained amplitude reduction factor S_0^2 value (1.00) was set in the EXAFS analysis to determine the coordination numbers (CNs) in the Co-O and Co-Co scattering path in sample.

**DFT Calculation**

All spined calculations are performed in the framework of the density functional theory with the projector augmented plane-wave method, as implemented in the Vienna ab initio simulation package.[S3] The generalized gradient approximation proposed by Perdew, Burke, and Ernzerhof is selected for the exchange-correlation potential.[S4] The long range van der Waals interaction is described by the DFT-D3 approach[S5] The cut-off energy for plane wave is set to 450 eV. The energy criterion is set to 10-5 eV in iterative solution of the Kohn-Sham equation. The structural models were built according to the experimental data. A slab p(11 Å × 11 Å × 25 Å) was used, and Brillouin zone integration was accomplished by Monkhorst-Pack k-point (2×2×1) mesh to simulate the two kinds of materials (Co_3O_4, V_O-$Mo_XCo_{3-X}O_4$). A vacuum layer of >15 Å is added perpendicular to the sheet to avoid artificial interaction between periodic images. All the structures are relaxed until the residual forces on the atoms have

declined to less than 0.03 eV/Å. The Gibbs free energy change was obtained based on the widely accept OER four-electron transfer mechanism according to the previous report.[S6, S7]

Additional Figures

The XRD patterns of the intermediates for synthesizing V_O-$Mo_XCo_{3-X}O_4$ and Co_3O_4 after hydrothermal treatment are shown in Figure S1. As a result, the phase of cobalt hydroxide ($Co(OH)_2$) is generated as a intermediate after hydrothermal treatment for further fabricating Co_3O_4. It can be found that the diffraction peaks of the intermediate for preparing V_O-$Mo_XCo_{3-X}O_4$ slightly left-shift to the lower angles when compared with that for Co_3O_4. It indicates that Mo, with a larger radius, is doped into the lattice of $Co(OH)_2$.
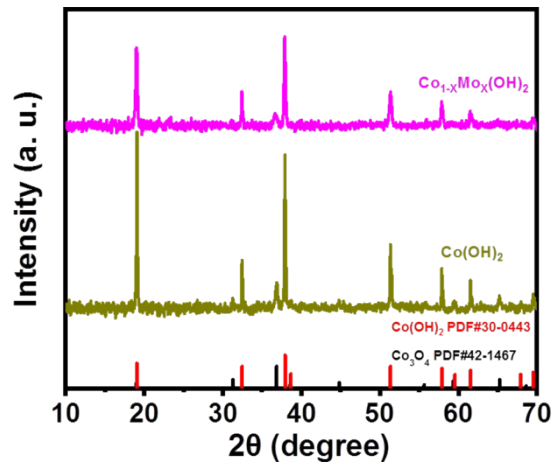
Figure S1. XRD patterns of the intermediates for synthesizing V_O-$Mo_XCo_{3-X}O_4$ and Co_3O_4 after hydrothermal treatment.

In Figure S2, it can be noticed that the peak position of A_{1g} in V_O-$Mo_XCo_{3-X}O_4$ shifts to a lower frequency compared to that of Co_3O_4.
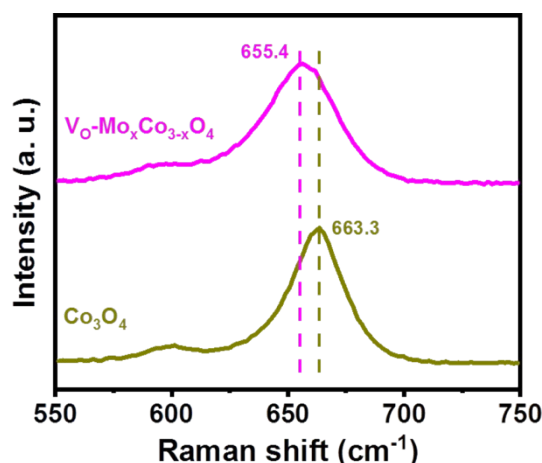
Figure S2. The Local Raman spectroscopy of V_O-$Mo_XCo_{3-X}O_4$ and Co_3O_4.

The FT-IR spectra of V_O-$Mo_XCo_{3-X}O_4$ and Co_3O_4 are shown in Figure S3. Distinctive broad bands around 3426 cm^{-1} were found on the FT-IR spectra, which mainly originate from the O-H scaling vibration of hydrogen-bonded water molecules.[S8] The δH_2O vibration was also observed at 1632 cm^{-1}.[S9] The FT-IR bands observed at 663 and 576 cm^{-1} are characteristic of the Co-O stretching vibration.[S10] The band at 663 cm^{-1} is attributed to the stretching vibration of the tetrahedral Co^{2+}-O bond, and the band at 576 cm^{-1} corresponds to the stretching peak of the octahedral Co^{3+}-O bond. In particular, the stretching peak of the Co^{3+}-O bond at 566 cm^{-1} for V_O-$Mo_XCo_{3-X}O_4$ is found to significantly shift to a lower frequency, indicating that Mo heteroatoms are doped into the octahedral sites.
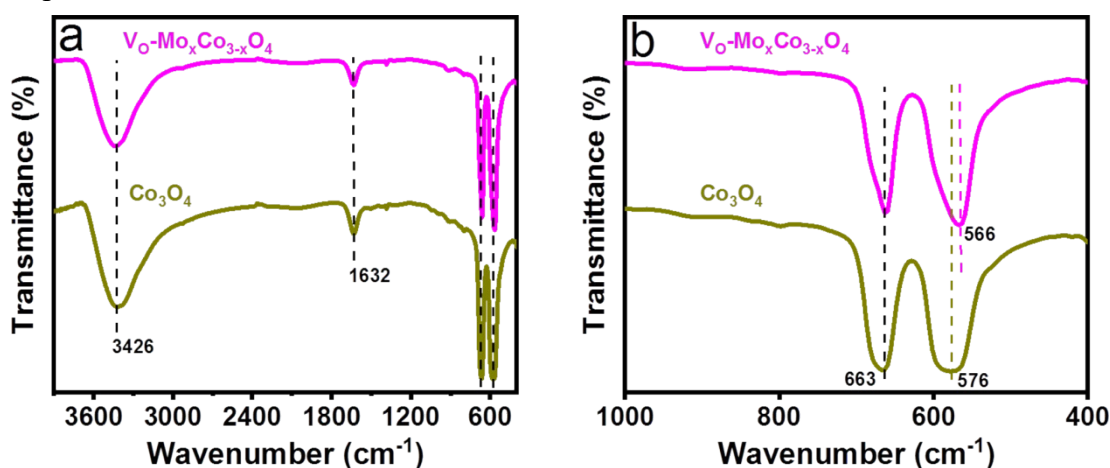
Figure S3. FT-IR spectra of V_O-$Mo_XCo_{3-X}O_4$ and Co_3O_4.

SEM and TEM images of Co_3O_4 are shown in Figure S4. As shown in Figure S4, SEM image of Co_3O_4 exhibits Co_3O_4 nanoparticles with sizes from 50-500 nm. Figure S4b

presents the HR-TEM image of Co_3O_4 edges. The crystal indices of 0.28 and 0.24 nm correspond to the (220) and (311) faces of Co_3O_4, respectively (Figure S4c). Based on the HAADF-STEM and corresponding elemental mapping images, a homogeneous distribution of cobalt and O in Co_3O_4 can be observed (Figure S4d-f).
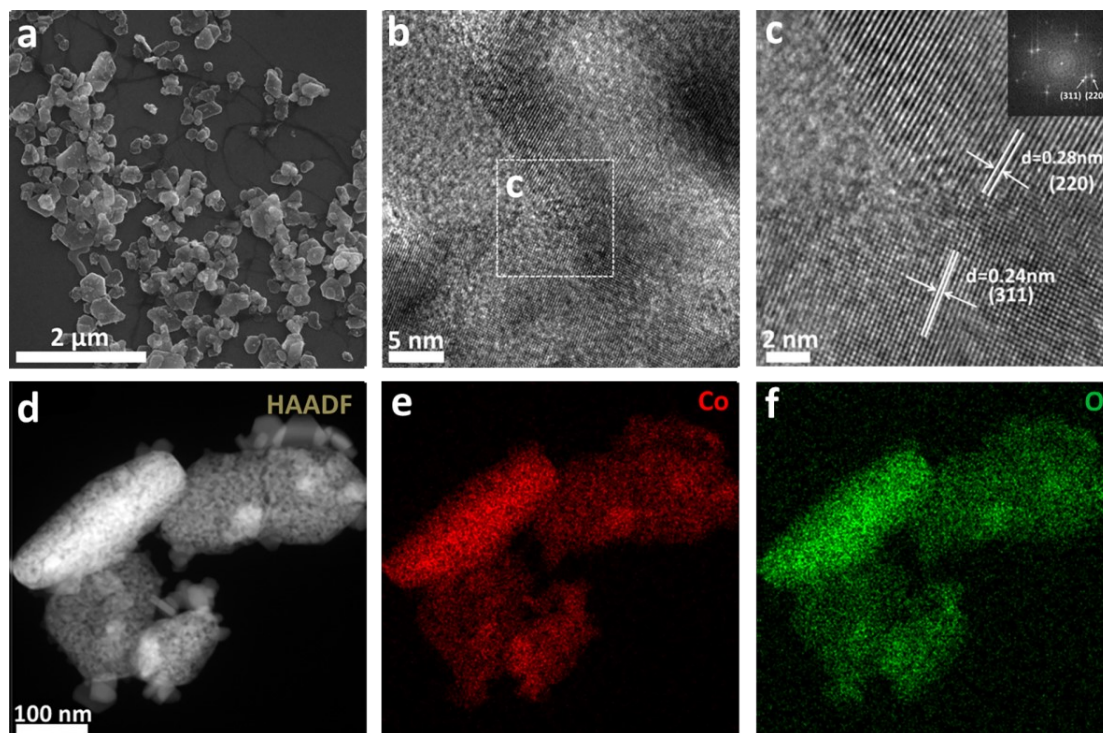

Figure S4. (a) SEM image of Co_3O_4 (b, c) HR-TEM images of Co_3O_4. (d-f) HAADF-STEM and corresponding elemental mapping images of Co_3O_4.
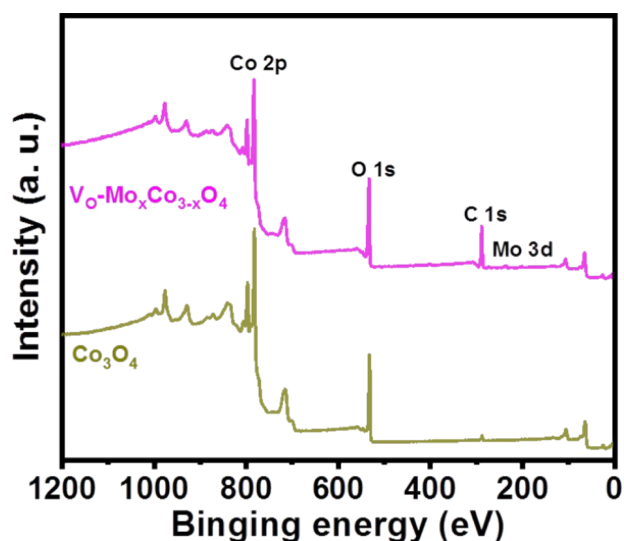
Figure S5. XPS survey spectra of V_O-$Mo_XCo_{3-X}O_4$ and Co_3O_4.

The XPS spectra of V_O-$Mo_XCo_{3-X}O_4$ and Co_3O_4 in Co 2p are shown in Figure S6, where

the BEs of 780.7 and 796.2 eV can be attributed to Co^{2+},[S11] and the BEs of 782.4 and 798.4 eV are attributed to the binding energy associated with the Co^{3+}.[S12]
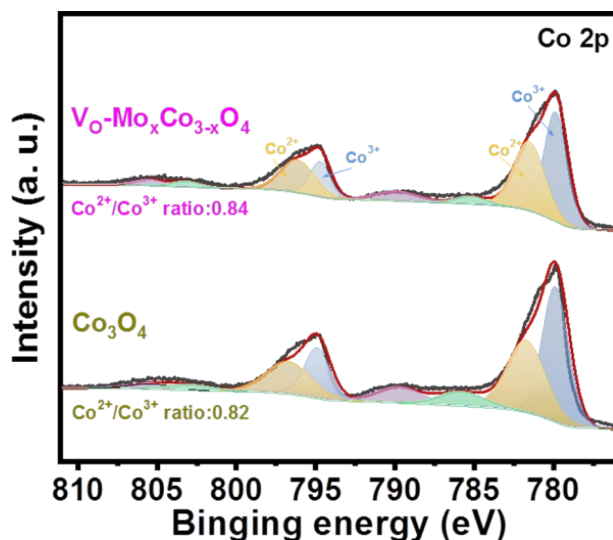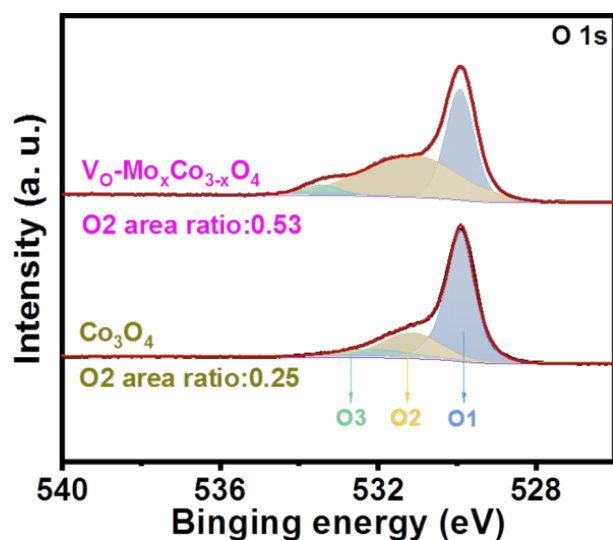

Figure S6. XPS spectra of V_O-$Mo_X Co_{3-X} O_4$ and $Co_3 O_4$ in Co 2p.

As shown in Figure S7, the XPS spectrum of V_O-$Mo_X Co_{3-X} O_4$ in Mo 3d can be decomposed into two sets of peaks, which are attributed to Mo^{4+} (231.6 and 234.7 eV) and Mo^{6+} (232.8 and 235.9 eV).[S13]
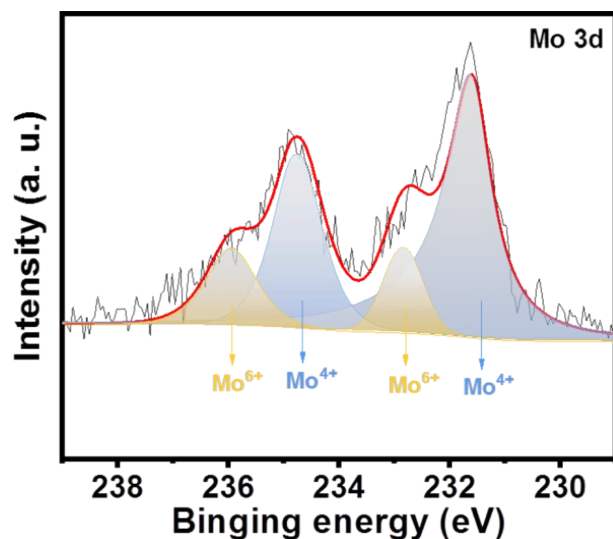

Figure S7. XPS spectra of V_O-$Mo_X Co_{3-X} O_4$ in Mo 3d.

The XPS spectra of V_O-$Mo_X Co_{3-X} O_4$ and $Co_3 O_4$ in O 1s are shown in Figure S8, where BEs of 530.4, 531.7, and 533.1 eV can be assigned to lattice oxygen (O1), oxygen vacancies (O2), and surface adsorbed water species (O3).[S14] The spectrum of V_O-$Mo_X Co_{3-X} O_4$ in O 1s exhibits a higher concentration of oxygen vacancies (O2) when compared with that of $Co_3 O_4$.

Figure S8. XPS spectra of V_O-$Mo_XCo_{3-X}O_4$ and Co_3O_4 in O 1s.
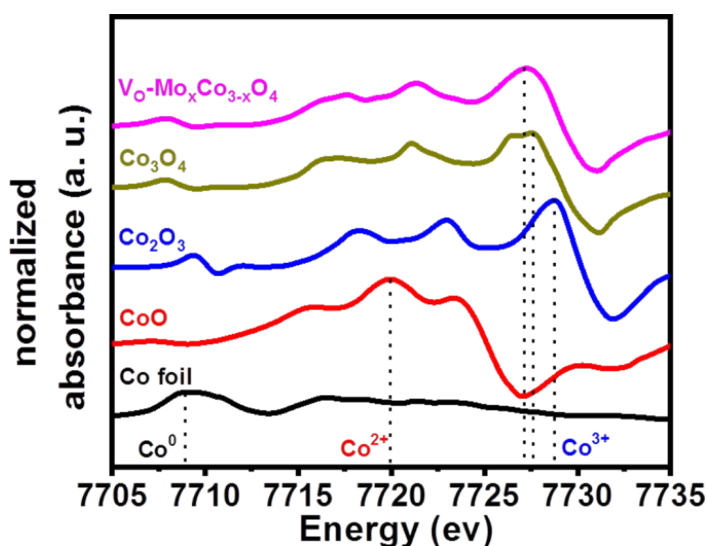
Figure S9. The first derivative of XANES spectra at Co K-edge of V_O-$Mo_XCo_{3-X}O_4$ and Co_3O_4 and reference materials.

The annealed temperature for preparing the V_O-$Mo_XCo_{3-X}O_4$ was optimized. The samples after hydrothermal treatment were washed and cleaned and then annealed under an air atmosphere at 200, 300, and 400 °C for 2 h, respectively. As displayed in Figure S10, the sample annealed at 300 °C exhibits the best activity towards OER in an acidic medium.
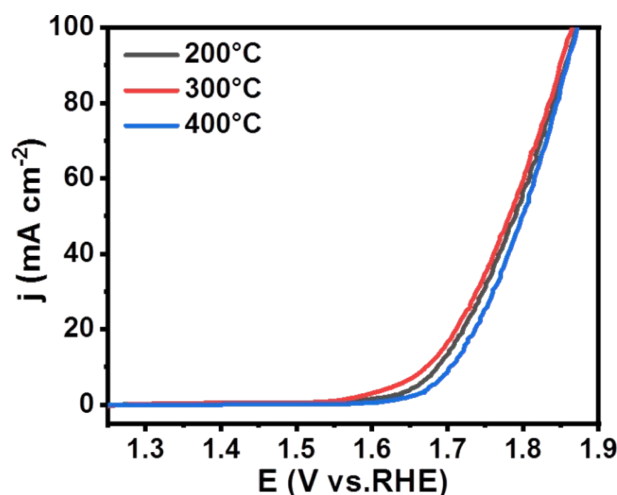
Figure S10. Polarization curves for different annealing temperatures.

It is well known that specific surface areas (ECSA) of electrocatalysts play an important role in the electrochemical reaction process. Thus, ECSA is considered an important parameter for evaluating performances of electrocatalysts and clarifying the origin of catalytic activity. Generally, ECSA is estimated through electrochemical double layer capacitance (C_{dl}) of electrocatalysts from CV curves in a non-Faradaic region with different scan rates:[S15]

$$C_{dl} = \frac{d(\Delta j)}{2dv}$$

In this formula, Δj represents the capacitive current density in selected potential on CV curves and v is corresponding to the scan rate. In a word, the slope of Δj against different scan rates can be used as a parameter for evaluating its ECSA.[S16] Relationships between Δj against different scan rates are obtained from corresponding CV cures on various electrocatalysts in 0.1 M $HClO_4$ Figure S11. As shown in Figure S11d, V_O-$Mo_XCo_{3-X}O_4$ shows a larger C_{dl} of 1.14 mF cm^{-2}. The loadings of Vo-$Mo_XCo_{3-X}O_4$ and Co_3O_4 on the electrodes for acidic OER are 1.0 mg cm^{-2}. For comparison, the loading of Ir on the electrode is 0.5 mg cm^{-2}. The ECSAs of Vo-$Mo_XCo_{3-X}O_4$, Co_3O_4, and Ir on the electrodes for acidic OER can be obtained according to the equation:

$$ECSA = \frac{C_{dl}}{C_S}$$

Where C_s is the specific capacitance of the electrode and we adopted the general

specific capacitance of $C_s = 0.040$ mF cm^{-2} based typical reported value.[S17] C_{dl} is the electrochemical double-layer capacitance of electrocatalysts, which can be estimated from CV curves in a non-Faradaic region with different scan rates.[S18]
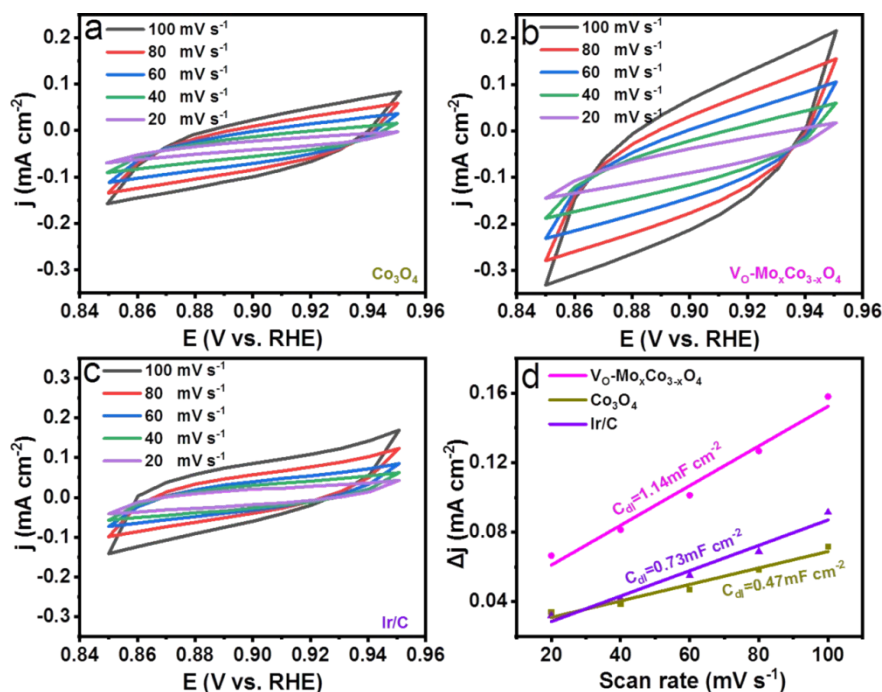
Figure S11. CV curves of (a) Co_3O_4, (b) V_O-$Mo_XCo_{3-X}O_4$, and (c) Ir/C electrocatalysts in 0.1 M $HClO_4$ from 0. 85 to 0.95 V vs. RHE with scan rates from 20 to 100 mV s^{-1} (d) Relationships between capacitive current densities (Δj) measured on various electrocatalysts against different scan rates in 0.1 M $HClO_4$.

The ECSA-normalized current densities of acidic OER on these electrocatalysts are obtained to measure the intrinsic activities, as shown in Figure S12a. As a result, at the overpotential of 470 mV, Vo-$Mo_XCo_{3-X}O_4$, Co_3O_4, and Ir/C exhibit ECSA-normalized current densities of 1.64, 0.64, and 0.28 mA cm^{-2}, respectively (Figure S12b). Therefore, Vo-$Mo_XCo_{3-X}O_4$ displays better intrinsic activity towards acidic OER compared with Ir/C.

Generally, octahedral cations are extensively regarded as the real active sites of spinel oxides for OER, because they are preferentially exposed on the near-surface.[S19, S20] Therefore, the tetrahedral cations are believed to have almost no contribution to the OER activity, owing to that they are relatively unlikely to be exposed on the surface.[S20, S21] To clarify the origination of the enhancement for acidic OER on the as-prepared Vo-

$Mo_XCo_{3-X}O_4$, the turnover frequency (TOFs) was calculated (Figure S12c). The TOF is a parameter of the instantaneous efficiency of a catalyst, which is calculated as the derivative of the number of turnovers of the catalytic cycle concerning the time per active site[S18]:

$$TOF = \frac{jA}{4Fm}$$

Where j (mA cm^{-2}) is the current density measured at the applied potential, A is the geometric area of an electrode, F is the Faraday constant (96,485 C mol^{-1}), and m is the mole number of the electrocatalyst on the electrode.[S18] The parameter of 4 refers to that four electrons are transferred for the generation of one O_2 molecule. As a result, at the overpotential of 470 mV, $Vo-Mo_XCo_{3-X}O_4$, Co_3O_4, and Ir/C present TOF values of 0.35, 0.14, and 0.19 O_2 s^{-1}, respectively (Figure S12d). $V_O-Mo_XCo_{3-X}O_4$ possesses a larger TOF value than that of Co_3O_4, indicating higher intrinsic activity of each active site. Thus, despite less active sites (octahedral cations), $V_O-Mo_XCo_{3-X}O_4$ achieves better activity towards acidic OER than Co_3O_4.

Additionally, the mass activities of acidic OER on $V_O-Mo_XCo_{3-X}O_4$, Co_3O_4, and Ir/C electrocatalysts have been studied as well (Figure S12e). As a result, $V_O-Mo_XCo_{3-X}O_4$ and Co_3O_4 exhibit mass activities of 62.56 and 10.61 mA mg-1 Co_3O_4 at the overpotential of 470 mV (Figure S12f). Ir/C displays a mass activity of 12.78 mA mg-1 Ir at the overpotential of 470 mV. Thus, $Vo-Mo_XCo_{3-X}O_4$ possesses a higher intrinsic activity towards acidic OER compared with Ir/C.
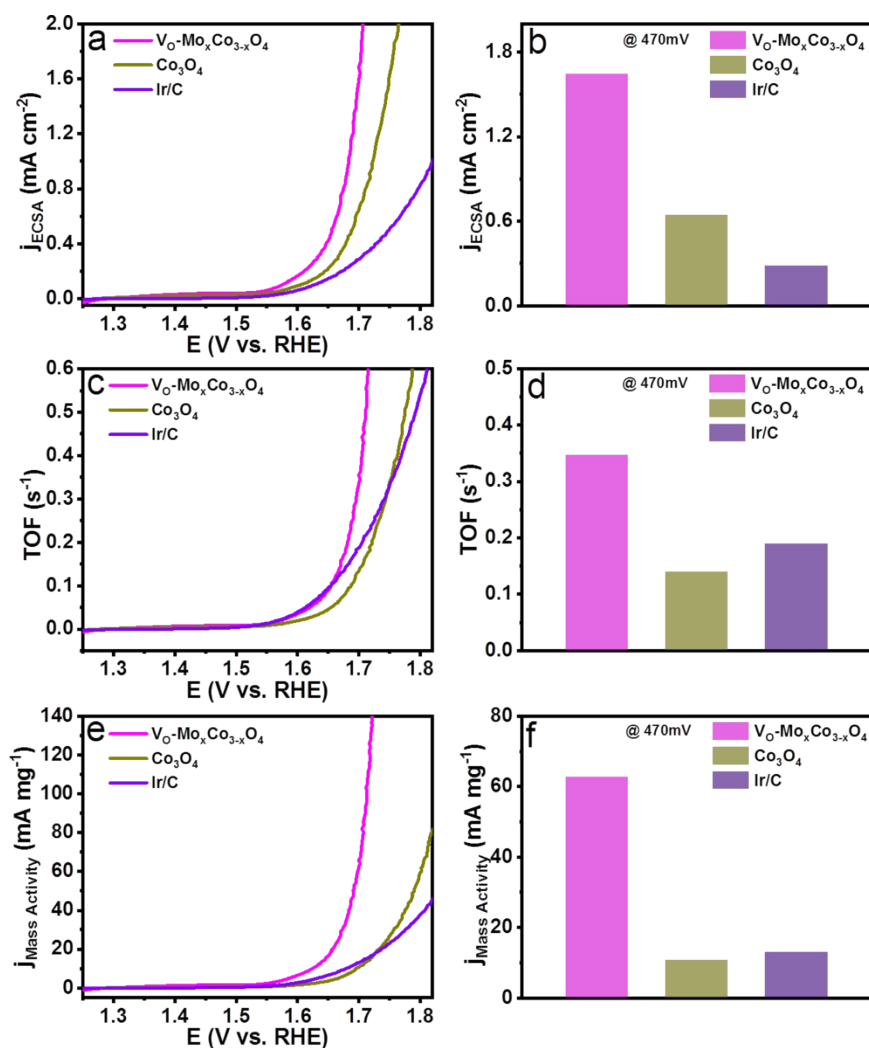
Figure S12. (a) ECSA-normalized polarization curves of OER on V_O-$Mo_XCo_{3-X}O_4$, Co_3O_4, and Ir/C electrocatalysts. (b) Corresponding ECSA-normalized specific current density of V_O-$Mo_XCo_{3-X}O_4$, Co_3O_4, and Ir/C for acidic OER at the overpotential of 470 mV. (c) TOF curves of OER on V_O-$Mo_XCo_{3-X}O_4$, Co_3O_4, and Ir/C electrocatalysts. (d) Corresponding TOF values of V_O-$Mo_XCo_{3-X}O_4$, Co_3O_4, and Ir/C for acidic OER at the overpotential of 470 mV. (e) The mass-normalized OER polarization curves of curves of OER on V_O-$Mo_XCo_{3-X}O_4$, Co_3O_4, and Ir/C electrocatalysts. (f) Corresponding mass activity values of V_O-$Mo_XCo_{3-X}O_4$, Co_3O_4, and Ir/C for acidic OER at the overpotential of 470 mV.

As shown in Figure S13, the Nyquist plot of V_O-$Mo_XCo_{3-X}O_4$ exhibits a smaller radius than that of Co_3O_4. Although constructing defects will increase the electronic resistance of a material, the radius is determined by the charge transfer resistance (reaction resistance), rather than intrinsic resistance.[S22, S23] Furthermore, the Nyquist plots of V_O-

13

$Mo_XCo_{3-X}O_4$ and Co_3O_4 are fitted by the two-time constant model, as shown in Table S4.[S20] As a result, V_O-$Mo_XCo_{3-X}O_4$ (1.31 Ω) and Co_3O_4 (1.34 Ω) exhibit similar values of solution resistance (R_s) because the same three-electrode-system was used for the electrochemical measurements. V_O-$Mo_XCo_{3-X}O_4$ (1.26 Ω) shows a smaller charge transfer resistance (R_{ct}) than Co_3O_4 (2.40 Ω), owing to the faster kinetics of the OER process through the OPM pathway.
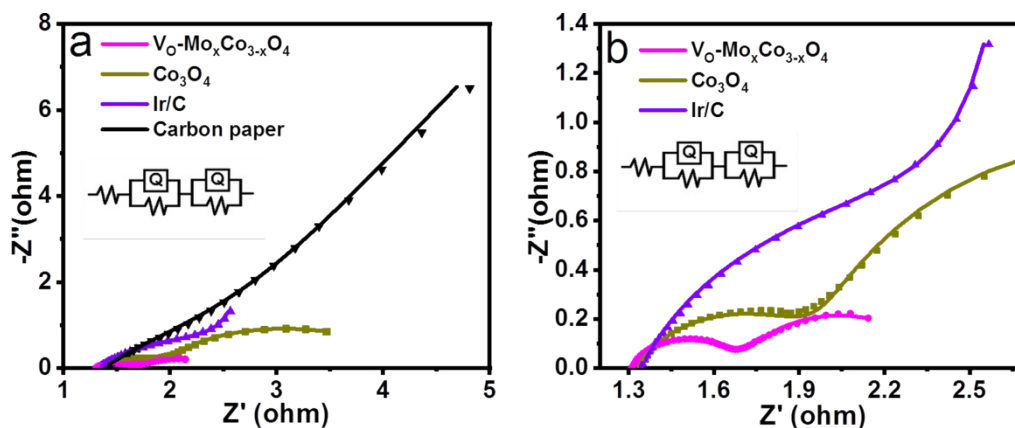
Figure S13. Nyquist plots of Co_3O_4, V_O-$Mo_XCo_{3-X}O_4$, Ir/C and carbon paper.

The XRD, SEM, XPS, and TEM characterizations have been performed to investigate the structural stability of V_O-$Mo_XCo_{3-X}O_4$ after the stability test (Figure S14-17). The XRD pattern, XPS spectrum, and morphology of V_O-$Mo_XCo_{3-X}O_4$ after stability test remains unchanged, indicating a high structural stability.
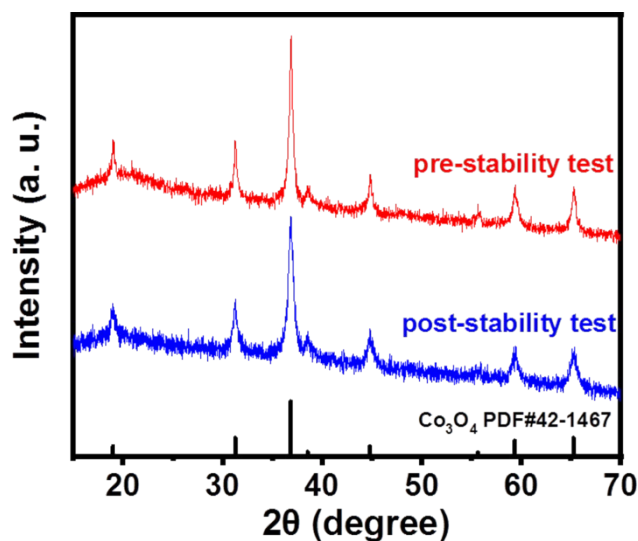
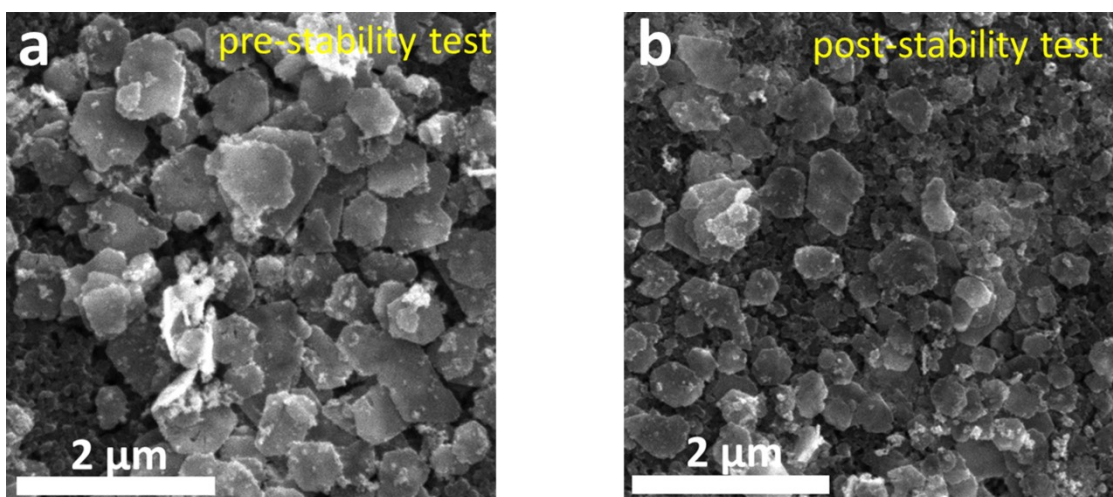**Figure S14.** XRD patterns of V_O-$Mo_XCo_{3-X}O_4$ before and after the stability test.

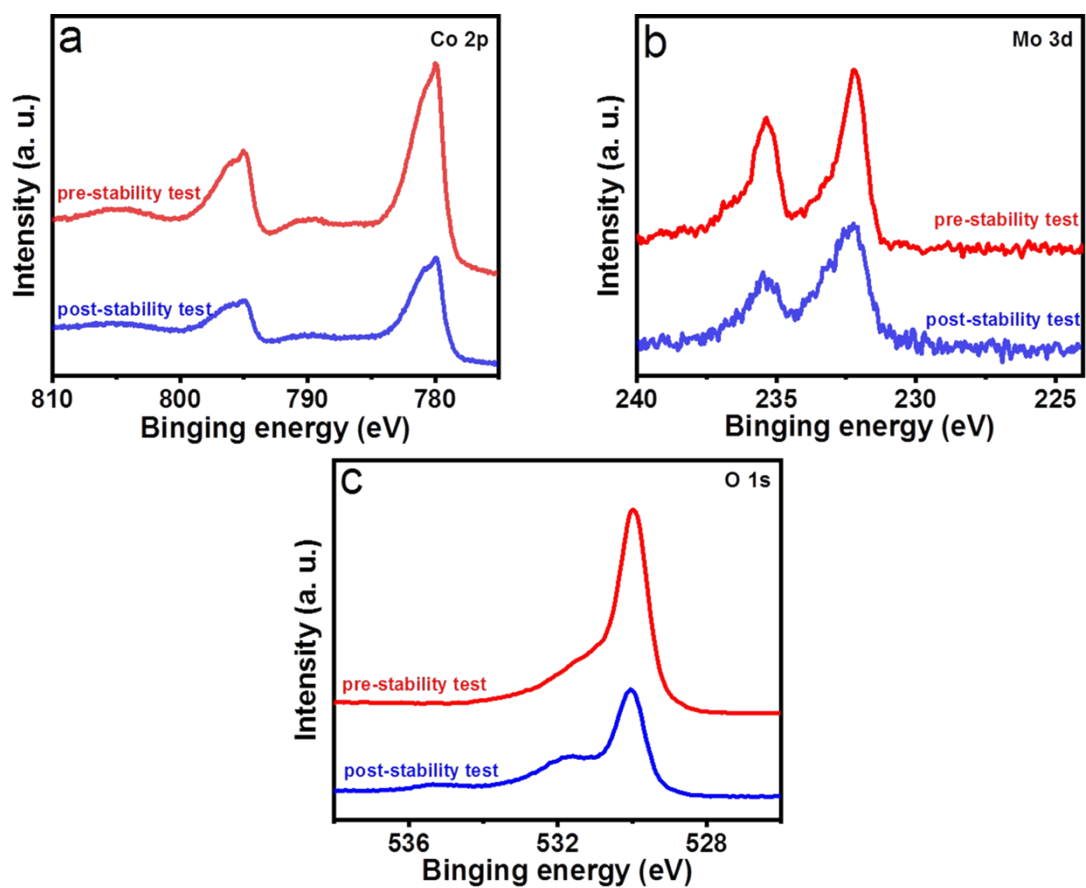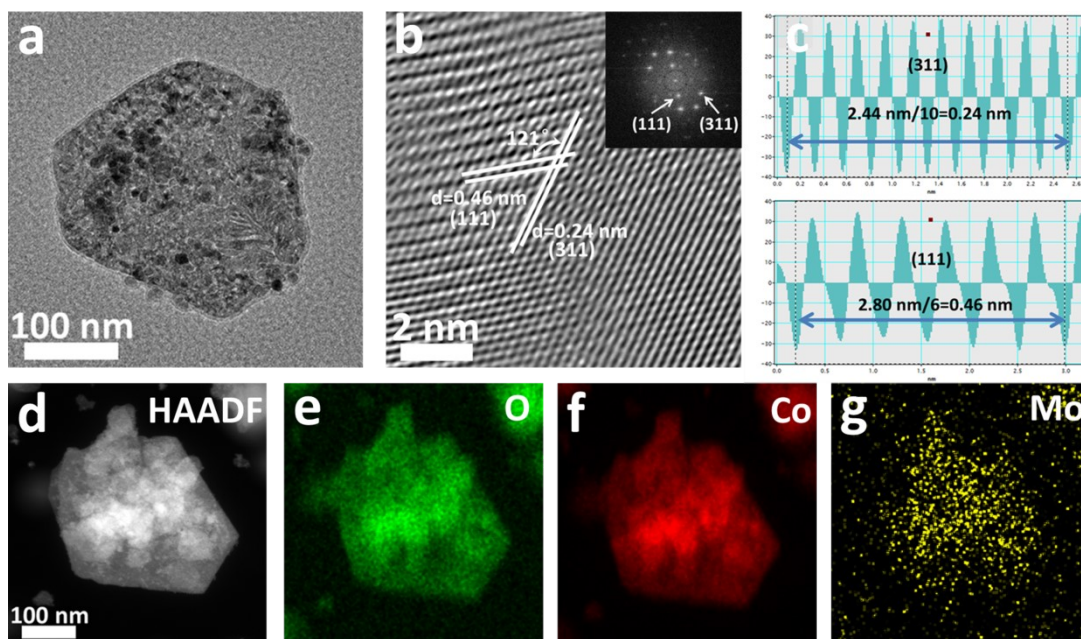**Figure S15.** The SEM images of V_O-$Mo_XCo_{3-X}O_4$ before and after stability test.

Figure S16. XPS spectras of V_O-$Mo_XCo_{3-X}O_4$ before and after stability test.

Figure S17. (a, b) The TEM images of V_O-$Mo_XCo_{3-X}O_4$ after the stability test. (c) Intensity profiles of the *d*-spacing for the (311) and (111) facets of V_O-$Mo_XCo_{3-X}O_4$ after the stability test. (d-g) HAADF-STEM and corresponding elemental mapping images of V_O-$Mo_XCo_{3-X}O_4$ after the stability test.
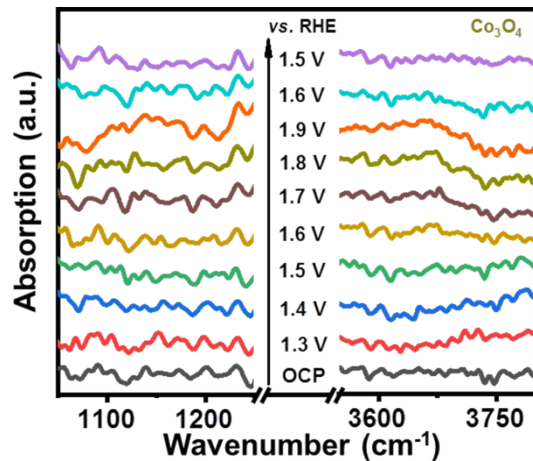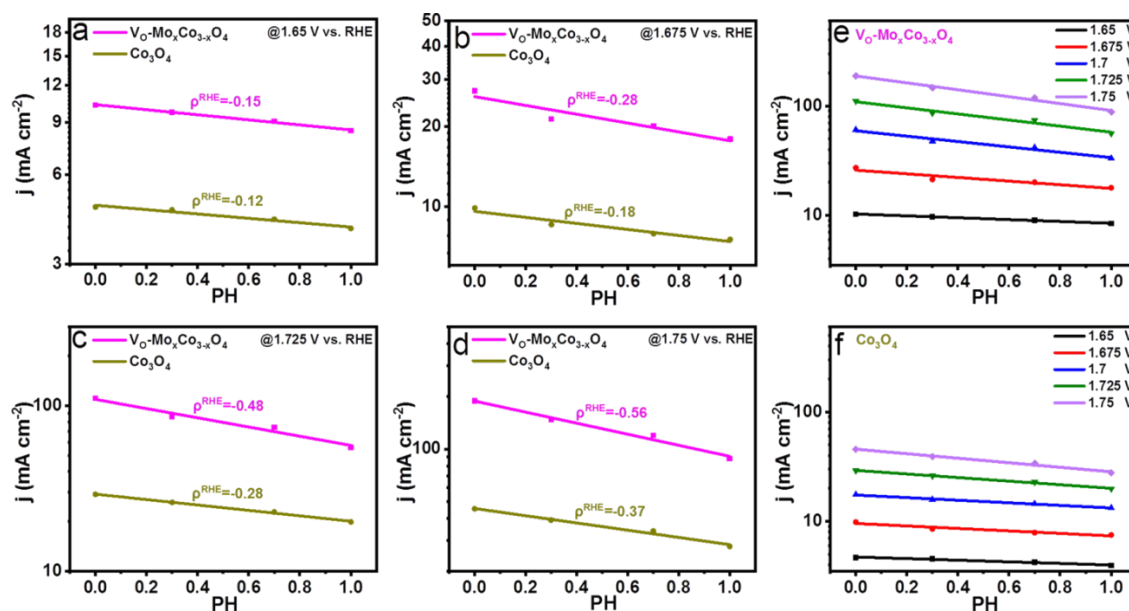

Figure S18. *In situ* FT-IR spectra recorded at various applied potentials (*vs*. RHE) in 0.1 M $HClO_4$ electrolyte on Co_3O_4.
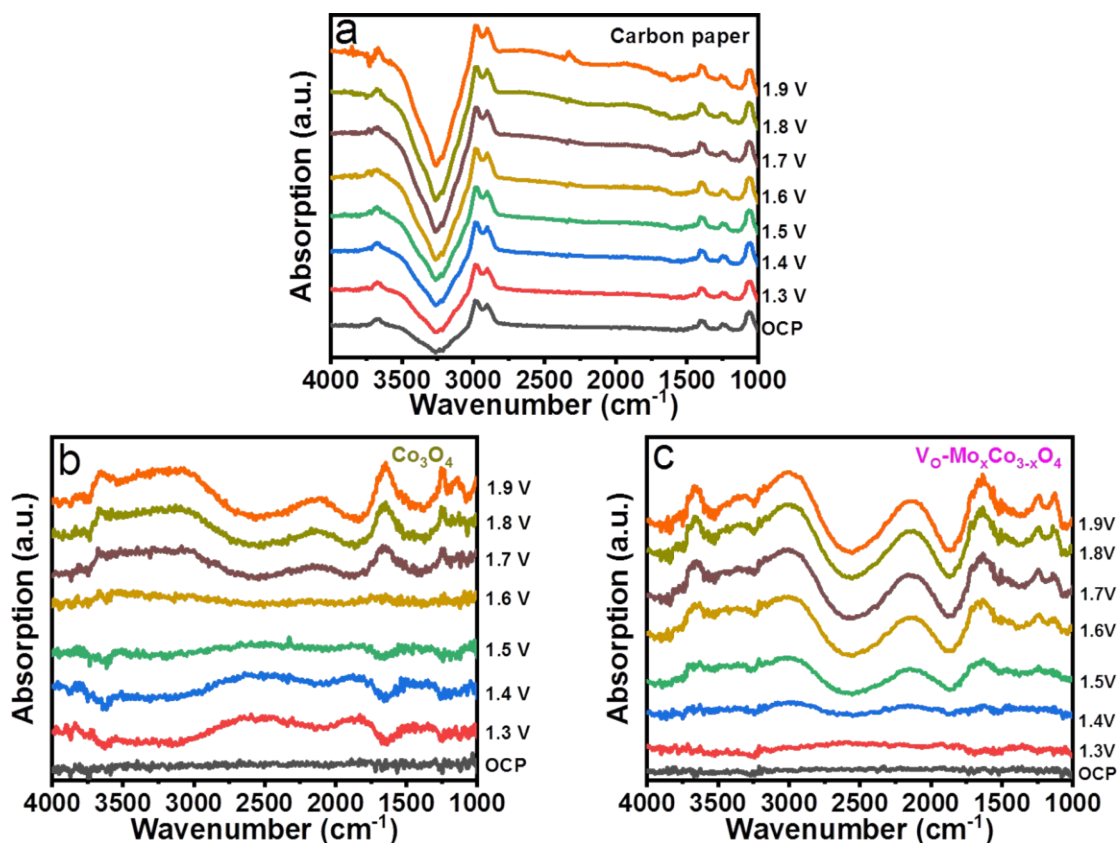
Figure S19. *In situ* FT-IR spectra of carbon paper, Co_3O_4 and V_O-$Mo_XCo_{3-X}O_4$ at various constant potentials (*vs*. RHE).

Figure S20. (a-d) OER specific activities of Co_3O_4, and V_O-$Mo_XCo_{3-X}O_4$ at 1.650, 1.675, 1.725, and 1.750 V against the different pH values. OER specific activities of (e) V_O-$Mo_XCo_{3-X}O_4$ and (f) Co_3O_4 obtained at different potentials against pH values.

As shown in Figure S21a, distinctive adsorption bands at about 503 cm^{-1} can be detected

on the *in situ* Raman spectra of Co_3O_4 measured above 1.6 V (*vs*. RHE), which is related to the generation of *OOH, the key intermediate of the AEM pathway.[S24, S25] However, similar bands can not be detected on the *in situ* Raman spectra of Vo-$Mo_XCo_{3-X}O_4$. It means that the generated species of *O-O* and *O-O detected on the *in situ* FTIR spectra of Vo-$Mo_XCo_{3-X}O_4$ are not from the *OOH species (Figure S21b). Generally, it has been extensively demonstrated that the distinctive intermediates of *O-O* and *O-O during the OPM pathway are from direct oxygen radical self-coupling to be oxygen bridge. Thus, the detection of *O-O* and *O-O species is usually regarded as direct evidence for triggering the OPM pathway during the OER process.
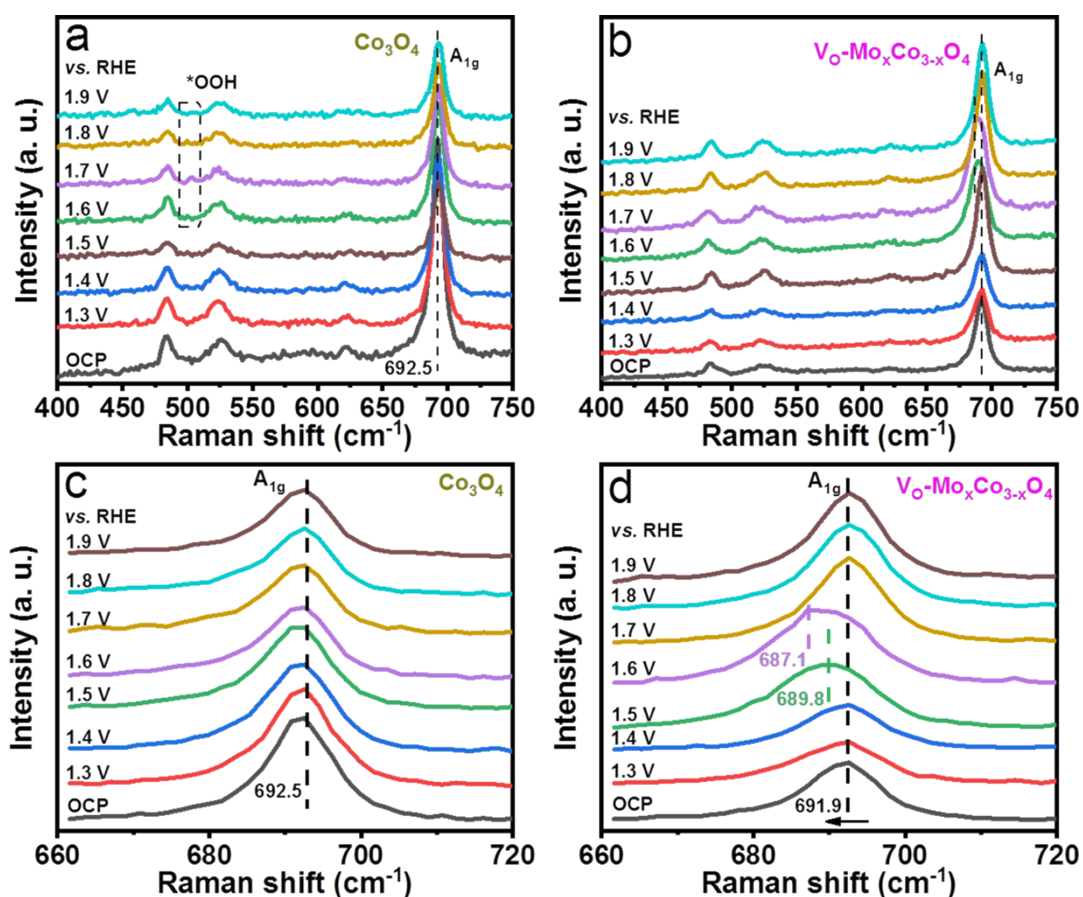
Figure S21. *In situ* Raman spectra of (a) Co_3O_4 and (b) V_O-$Mo_XCo_{3-X}O_4$ at various applied potentials (*vs*. RHE). The A_{1g} mode on the *in situ* Raman spectra of (c) Co_3O_4 and (d) V_O-$Mo_XCo_{3-X}O_4$ obtained during stepping the potential from OCP to 1.9 V *vs*. RHE in 0.1 M $HClO_4$ electrolyte.
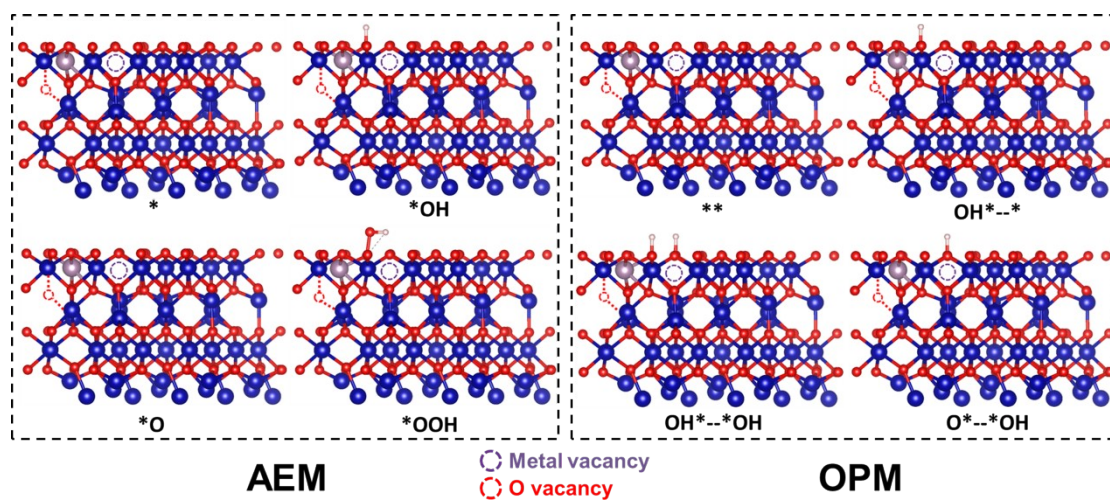
Figure S22. Optimized structures of key intermediates of V_O-$Mo_XCo_{3-X}O_4$ for the AEM and OPM in the OER process
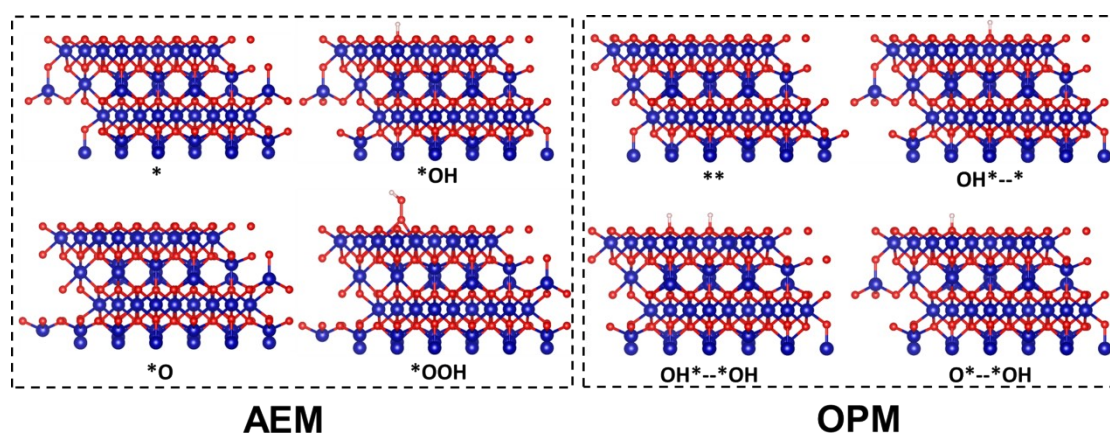
Figure S23. Optimized structures of key intermediates of Co_3O_4 for the AEM and OPM in the OER process
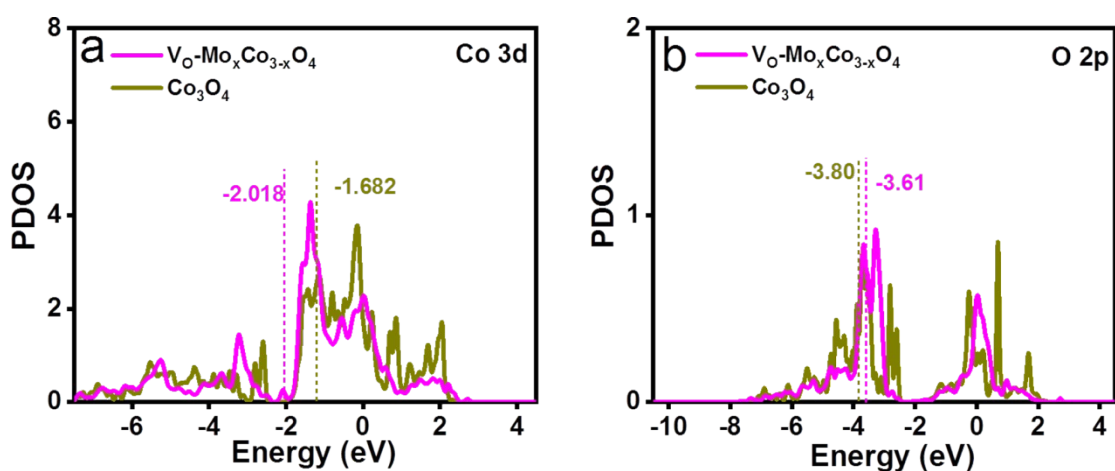
Figure S24. (a) Comparison of the Co $3d$-band center of V_O-$Mo_XCo_{3-X}O_4$ and Co_3O_4. (b) Comparison of the O $2p$-band center of V_O-$Mo_XCo_{3-X}O_4$ and Co_3O_4.

19

Additional Table

According to the results of XPS spectroscopy, the atomic ratio of Mo to Co in the near-surface of V_O-$Mo_XCo_{3-X}O_4$ is obtained to be 3:247 (Table S1). Based on the result of ICP, the total atomic ratio of Mo to Co in V_O-$Mo_XCo_{3-X}O_4$ is 1:230. Therefore, Mo cations should mainly distribute in the near-surface of V_O-$Mo_XCo_{3-X}O_4$.

Table S1. The atomic ratio of Mo to Co in the near-surface of V_O-$Mo_XCo_{3-X}O_4$ detected from XPS spectroscopy.

Element	Element Atomic %
Co	98.77
Mo	1.23

Table S2. Fitting parameters in the Co K-edge EXAFS for V_O-$Mo_XCo_{3-X}O_4$ and Co_3O_4.

Sample	Shell	CN^a	$R(Å)^b$	$\sigma^2(Å^2)^c$	$\Delta E_0(eV)^d$	R-factor
V_O-$Mo_xCo_{3-x}O_4$	Co_{oct}-O	4.122	1.880	0.00029	-5.99741	0.00715
	Co_{td}-O	5.375	1.994	0.00218		
	Co_{oct}-TM_{oct}	5.598	2.869	0.00634		
	Co_{td}-TM_{oct}	9.982	3.361	0.00628		
	Co_{td}-TM_{td}	4.086	3.504	0.00008		
Co_3O_4	Co_{oct}-O	4.107	1.824	0.00455	-6.05066	0.00110
	Co_{td}-O	6.160	1.953	0.00038		
	Co_{oct}-Co_{oct}	6.257	2.861	0.00628		
	Co_{td}-Co_{oct}	10.859	3.365	0.00500		
	Co_{td}-Co_{td}	4.125	3.518	0.00361		

As shown in Table S3, it should be noted that most of these state-of-the-art non-precious metal electrocatalysts were tested in electrolytes with a pH value of 0 (1.0 M $HClO_4$ or 0.5 M H_2SO_4), while we adopted an electrolyte of 0.1 M $HClO_4$ (pH=1) for the measurements. This is because the pH value in the working environment of a PEMWE is close to pH=1.[S26]

Table S3. The activity and kinetics of currently documented state-of-the-art non-precious metal electrocatalysts for acidic OER.

Electrocatalyst	Electrolyte	Tafel slope (mV dec^{-1})	η (mV) @ 10 mA cm^{-1}	Reference
V_O-$Mo_xCo_{3-x}O_4$	0.1 M $HClO_4$	102.5	420	*This work*

90-Co−MnO$_2$	0.1 M HClO$_4$	158	901	*Adv. Mater.* **2023**, 35, 2207066
Co$_3$O$_4$@rGO/CP	0.5 M H$_2$SO$_4$	121	380	*Chem. Eng. J.* **2023**, 451, 138471.
Co$_3$O$_4$-CoMoO$_4$	0.5 M H$_2$SO$_4$	87.8	410	*Chem. Eng. J.* **2023**, 473, 145353
Co$_{3-x}$Ba$_x$O$_4$	1 M HClO$_4$	30	281	*J. Am. Chem. Soc.* **2023**, 145, 7829
Co$_2$MnO$_4$/FTO	0.05 M H$_2$SO$_4$	79.6	395	*Nat. Catal.* **2022**, 5, 109
Co$_3$O$_4$@C/GPO	1 M H$_2$SO$_4$	143	360	*Nat. Commun.* **2022**, 13, 4341
Fe-Co$_3$O$_4$@C/FTO	0.5 M H$_2$SO$_4$	68.6	396	*Appl. Catal. B Environ* **2022**, 303, 120899
Co$_3$O$_4$/CeO$_2$	0.5 M H$_2$SO$_4$	88.1	423	*Nat. Commun.* **2021**, 12, 3036
P-Co$_3$O$_4$/GC	0.1 M HClO$_4$	98	400	*J. Colloid Interface Sci.* **2023**, 641, 329
Co$_3$O$_4$@N-C/FTO	0.5 M H$_2$SO$_4$	152	465	*J. Colloid Interface Sci.* **2022**, 623, 327

Table S4. R$_s$ and R$_{ct}$ were obtained by fitting the Nyquist plot of Co$_3$O$_4$ and V$_O$-Mo$_x$Co$_{3-X}$O$_4$ at 1.7 *vs*. RHE.

Electrocatalyst	R$_s$ (Ω)	R$_{ct}$ (Ω)
V$_O$-Mo$_x$Co$_{3-x}$O$_4$	1.31	1.26
Co$_3$O$_4$	1.34	2.40

Most reported electrocatalysts (including precious metal based electrocatalysts) are usually only able to stably catalyze the acidic OER for a few tens of hours (Table R3). The as-prepared V$_O$-Mo$_x$Co$_{3-x}$O$_4$ is at a similar level compared with the current reported state-of-the-art electrocatalysts in stability for acidic OER.

Table S5. Comparisons of stability for acidic OER on reported state-of-the-art Co-based electrocatalysts

Electrocatalyst	Electrolyte	Stability	Reference

V_O-$Mo_xCo_{3-x}O_4$	0.1 M $HClO_4$	Maintaining 10 mA cm^{-2} for 30 h	*This work*
$Ir_{lat}@Co_3O_4$	0.5 M H_2SO_4	Maintaining 98.3% of activity @10 mA cm^{-2} after 12 h	*J. Energy Chem.* **2024**, *89*, 355
$Ru_{(anc)}$-Co_3O_4	0.5 M H_2SO_4	Maintaining 10 mA cm^{-2} for 150 h	*J. Am. Chem. Soc.* **2023**, *145*, 23659
Co−Co DASs/ZCC	0.5 M H_2SO_4	Maintaining 10 mA cm^{-2} for 40 h	*Angew. Chem. Int. Ed.* **2023**, *62*, e202314185
Ru-Co_3O_4	0.5 M H_2SO_4	Maintaining 10 mA cm^{-2} for 16.5 h	*J. Mater. Chem. A*, **2023**, *11*, 21767
Co_3O_4/$CoRuO_x$	0.1 M $HClO_4$	Maintaining 10 mA cm^{-2} for 36 h	*Small* **2023**, *19*, 2204889
$Co_{3-x}Ba_xO_4$	0.5 M H_2SO_4	Maintaining 10 mA cm^{-2} for 110 h	*J. Am. Chem. Soc.* **2023**, *145*, 7829
LaMn@Co-ZIF	0.1 M $HClO_4$	Maintaining 10 mA cm^{-2} for 353 h	*Science* **2023**, *380*, 609
Ir-Co_3O_4	0.5 M H_2SO_4	Maintaining 10 mA cm^{-2} for 30 h	*Nat. Commun.* **2022**, *13*, 7754
Co_3O_4@C/GPO	1 M H_2SO_4	Maintaining 10 mA cm^{-2} for 43 h	*Nat. Commun.* **2022**, *13*, 4341
Co_3O_4/CeO_2	0.5 M H_2SO_4	Potential to maintain 10 mA cm^{-2} increases by 60 mV in 50 h	*Nat. Commun.* **2021**, *12*, 3036

References

S1   B. Ravel and M. Newville, *J. Synchrotron Radiat.*, 2005, **12**, 537-541.

S2   S. I. Zabinsky, J. J. Rehr, A. Ankudinov, R. C. Albers and M. J. Eller, *Physical Review B*, 1995, **52**, 2995-3009.

S3   G. Kresse and D. Joubert, *Physical Review B*, 1999, **59**, 1758-1775.

S4   J. P. Perdew, K. Burke and M. Ernzerhof, *Phys. Rev. Lett.*, 1996, **77**, 3865-3868.

S5   S. Grimme, J. Antony, S. Ehrlich and H. Krieg, *J. Chem. Phys.*, 2010, **132**, 154104.

S6   H. You, D. Wu, D. Si, M. Cao, F. Sun, H. Zhang, H. Wang, T.-F. Liu and R. Cao, *J. Am. Chem. Soc.*, 2022, **144**, 9254-9263.

S7   C. Lin, J.-L. Li, X. Li, S. Yang, W. Luo, Y. Zhang, S.-H. Kim, D.-H. Kim, S. S. Shinde, Y.-F. Li, Z.-P. Liu, Z. Jiang and J.-H. Lee, *Nat. Catal.*, 2021, **4**, 1012-1023.

S8   S. Zhao, Z. Wang, H. Kang, W. Zhang, J. Li, S. Zhang, L. Li and A. Huang, *Chem. Eng. J.*, 2019, **359**, 275-284.

S9   G. Solomon, A. Landström, R. Mazzaro, M. Jugovac, P. Moras, E. Cattaruzza, V. Morandi, I. Concina and A. Vomiero, *Adv. Energy Mater.*, 2021, **11**, 2101324.

S10   J. Lv, L. Wang, R. Li, K. Zhang, D. Zhao, Y. Li, X. Li, X. Huang and G. Wang, *ACS Catal.*, 2021, **11**, 14338-14351.

S11. L. Lv, D. Zha, Y. Ruan, Z. Li, X. Ao, J. Zheng, J. Jiang, H. M. Chen, W.-H. Chiang, J. Chen and C. Wang, *ACS Nano*, 2018, **12**, 3042-3051.

S12   Y. Fang, Y. Xue, Y. Li, H. Yu, L. Hui, Y. Liu, C. Xing, C. Zhang, D. Zhang, Z. Wang, X. Chen, Y. Gao, B. Huang and Y. Li, *Angew. Chem. Int. Ed.*, 2020, **59**, 13021-13027.

S13   M. Zang, N. Xu, G. Cao, Z. Chen, J. Cui, L. Gan, H. Dai, X. Yang and P. Wang, *ACS Catal.*, 2018, **8**, 5062-5069.

S14   L. Zhuang, L. Ge, Y. Yang, M. Li, Y. Jia, X. Yao and Z. Zhu, *Adv. Mater.*, 2017, **29**, 1606793.

S15   J. Bao, X. Zhang, B. Fan, J. Zhang, M. Zhou, W. Yang, X. Hu, H. Wang, B. Pan and Y. Xie, *Angew. Chem. Int. Ed.*, 2015, **54**, 7399-7404.

S16   A. Sivanantham, P. Ganesan and S. Shanmugam, *Adv. Funct. Mater.*, 2016, **26**, 4661-4672.

S17   Y. Zhu, J. Wang, T. Koketsu, M. Kroschel, J. M. Chen, S. Y. Hsu, G. Henkelman, Z. Hu, P. Strasser and J. Ma, *Nat. Commun.*, 2022, **13**, 7754.

S18   L. Chong, G. Gao, J. Wen, H. Li, H. Xu, Z. Green, J. D. Sugar, A. J. Kropf, W.

Xu, X. M. Lin, H. Xu, L. W. Wang and D. J. Liu, *Science*, 2023, **380**, 609-616.

S19 R. Chen, Z. Wang, S. Chen, W. Wu, Y. Zhu, J. Zhong and N. Cheng, *ACS Energy Lett.*, 2023, **8**, 3504-3511.

S20 Y. Peng, C. Huang, J. Huang, M. Feng, X. Qiu, X. Yue and S. Huang, *Adv. Funct. Mater.*, 2022, **32**, 2201011.

S21 Y. Zhou, S. Sun, C. Wei, Y. Sun, P. Xi, Z. Feng and Z. J. Xu, *Adv. Mater.*, 2019, **31**, e1902509.

S22 S. Anantharaj and S. Noda, *ChemElectroChem*, 2020, **7**, 2297-2308.

S23 Y. J. Wu, J. Yang, T. X. Tu, W. Q. Li, P. F. Zhang, Y. Zhou, J. F. Li, J. T. Li and S. G. Sun, *Angew. Chem. Int. Ed.*, 2021, **60**, 26829-26836.

S24 A. Moysiadou, S. Lee, C. S. Hsu, H. M. Chen and X. Hu, *J. Am. Chem. Soc.*, 2020, **142**, 11901-11914.

S25 W. H. Lee, M. H. Han, Y. J. Ko, B. K. Min, K. H. Chae and H. S. Oh, *Nat. Commun.*, 2022, **13**, 605.

S26 H. N. Nong, T. Reier, H.-S. Oh, M. Gliech, P. Paciok, T. H. T. Vu, D. Teschner, M. Heggen, V. Petkov, R. Schlögl, T. Jones and P. Strasser, *Nat. Catal.*, 2018, **1**, 841-851.